Chemical Engineering Science 280 (2023) 118982

Contents lists available at ScienceDirect

Chemical Engineering Science

journal homepage: www.elsevier.com/locate/ces

Pore-morphology-based pore structure characterization for various porous media

Zhipeng Xu [a,b], Mian Lin [b,c,*], Wenbin Jiang [b,c], Leige Xu [a], Lili Ji [b,c], Gaohui Cao [b], Wei Hao [d,*]

[a] School of Civil Engineering and Communication, North China University of Water Resources and Electric Power, Zhengzhou 450045, China
[b] Institute of Mechanics, Chinese Academy of Sciences, Beijing 100190, China
[c] School of Engineering Science, University of Chinese Academy of Sciences, Beijing 100049, China
[d] China France Bohai Geoservices Co., Ltd, Tianjin 300452, China

ARTICLE INFO

Keywords:
Pore structure characterization
Pore morphology
CT image
Mercury injection simulation
Gas pore condensation simulation

ABSTRACT

Quantitative characterization of pore structure plays an important role in predicting properties of porous media and it has significant applications in energy and chemical engineering. Mercury injection capillary pressure experiments and gas adsorption experiments are the major pore structure characterization techniques, but they are time-consuming, costly, and destructive. In this paper, a simple pore-morphology-based method is developed to simulate the mercury injection and gas pore condensation in CT image for obtaining the pore structure characteristics. The main idea of the developed algorithm is to utilize some of the morphological operations to capture the pore geometry and topology, and then combine with the invasion phase connectivity analysis to implement the mercury injection and gas pore condensation. The algorithm is designed in several ways with an improved computational speed and characterization accuracy. The algorithm is user-friendly and can be applied on 2D and 3D images. Various porous media are used to assess the performance of the algorithm and the characteristics of pore structures. The results are compared to the available results in the literature. Findings show that the algorithm can reliably quantitatively characterize the pore structure for a wide variety of porous media. The general pore radius distribution, pore throat radius distribution, and strict throat radius distribution involved in pore structure characterization are clarified. The characterization of heterogeneous pore structures and the effects of pore roughness on capillary pressure are discussed.

1. Introduction

Pore structure characteristics has a profound impact on macro properties of porous media, such as permeability and conductivity (An et al., 2016; Daigle et al., 2017; Hu et al., 2017; Fagbemi et al., 2018). The importance of pore structure characteristics can be observed in many engineering applications. In chemical engineering, the pore structure characteristics affect the flow of fluids in pore spaces (Ortiz-Landeros et al., 2013; He et al., 2020; Zhang et al., 2022). In energy and geosciences, the pore structure characteristics affect the transport of oil and gas, the identification of sweet spots, and the reservoir quality (Tahmasebi et al., 2017; Xu et al., 2020; Zeng et al., 2022).

Mercury injection capillary pressure (MICP) and gas adsorption (GD) are currently the major pore structure characterization techniques (Tsakiroglou et al., 2009; Okolo et al., 2015; Njiekak et al., 2018; Jiang et al., 2022). MICP is the process that mercury breaks through the corresponding throat and enters the pore spaces controlled by it with the gradual increase of injection pressure. Through counting the mercury injection volume at each injection pressure, the capillary pressure–saturation curve and the pore throat radius distribution can be obtained. The capillary pressure–saturation curve depends on the geometry and topology of pore space, and plays a significant role in many applications of porous media, such as the evaluations of pore space and the studies of two-phase flow (Sweijen et al., 2017). The pore throat radius distribution only reflects the throat size spectrum of porous media because the pores are controlled by the throats (Xu et al., 2020). GD is a significantly complicated physical process, which can be used to get the general pore radius distribution to supplement the pore throat radius distribution of MICP. The general pore radius distribution is calculated from the GD results using some adsorption models (Langmuir, 1917; Brunauer et al., 1938; Basha et al., 2008). Although the MICP and GD experiments are widely used for the pore structure

* Corresponding authors at: Institute of Mechanics, Chinese Academy of Sciences, Beijing 100190, China (M. Lin).
E-mail addresses: linmian@imech.ac.cn (M. Lin), haowei@cfbgc.com (W. Hao).

https://doi.org/10.1016/j.ces.2023.118982
Received 5 April 2023; Received in revised form 27 May 2023; Accepted 8 June 2023
Available online 14 June 2023

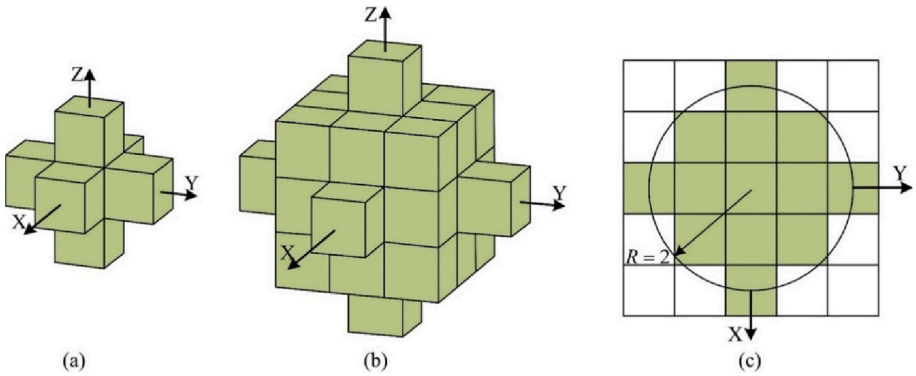

Fig. 1. Schematic of the spherical structure element (SSE). The SSE with (a) $R = 1$ and (b) $R = 2$. (c) A XY-cross section of the S_e, where the SSE with $R = 2$ is stored. The category of voxels inside SSE is opposite to that of voxels outside SSE.

characterization, they are time-consuming, costly, destructive, and less environment friendly.

Micro computerized tomography (CT) scanning is an efficient, non-invasive, and non-destructive 3D imaging technique, and has received increasing interest recently (Gooya et al., 2016; Jiang et al., 2017; Krakowska et al., 2018; Zhao et al., 2019; Meng, 2022). The 3D representation of the pore structure can be implemented in grayscale image. Through the threshold segmentation algorithm, it is possible to easily convert the grayscale image into the binary image, in which each element has a value of either 0 (solid voxel) or 1 (void voxel). The MICP and GD can be implemented numerically in the 3D binary image to characterize the pore structure.

Mathematical morphology method as a common 3D image processing method has been widely used for characterizing pore structures from CT image (Hilpert and Miller, 2001; Hilpert et al., 2003; Yang et al., 2015; Sweijen et al., 2017; Aslannejad et al., 2017; Xu et al., 2020). The method converts complex image processing computations into combinations of voxel conversions and logical operations based on the morphological theory presented by Matheron (1975) and Serra (1982). Through these morphological operations, such as dilation, erosion, opening and closing, the morphological and geometric properties of pore structures can be acquired. Compared with other image-based pore structure characterization approaches, the mathematical morphology method is a full-morphology algorithm without assumptions and artificial criteria (Xu et al., 2020), and can simply, intuitively, and conveniently characterize pore structures.

By combining with the invasion phase connectivity analysis, the mathematical morphology method can simulate the mercury injection process. In the MICP simulation, the air-mercury interface is represented by a hemisphere whose radius is related to capillary pressure. Then, for a given capillary pressure, all air-mercury interfaces with corresponding radius are identified in pore spaces by morphological operations, while the mercury phase connectivity analysis is implemented to maintain the connectivity of mercury phase to its injection. The capillary pressure increases from small to large and eventually, the capillary pressure–saturation curve is obtained. Hilpert and Miller (2001) used the approach to simulate the capillary pressure–saturation curve in sphere packing. Vogel et al. (2005) simulated the capillary pressure–saturation curve in the actual pore geometry via morphology method, and compared the result with these calculated by pore network method and Lattice Boltzmann method. Results showed that the capillary pressure–saturation curves predicted by morphology method and pore network method were similar, while Lattice Boltzmann method gave lower capillary pressure values. Yang et al. (2015) and Sweijen et al. (2017) used the morphology method to extract the capillary pressure–saturation curve from CT image of porous media. The existing MICP simulation is implemented on each voxel of image explicitly, which poses huge computational challenges. Moreover, the existing MICP simulation cannot distinguish the air-mercury interface in pore spaces with radius of 1 voxel and the pore spaces with radius of half voxel, because the spherical structure element employed in the simulation only possesses integer radii.

GD is a significantly complicated physical process. GD simulation is mainly implemented by Molecular Dynamics and Grand canonical Monte Carlo (Mosher et al., 2013; Chen et al., 2016; Xiong et al., 2016; Brasili et al., 2019). In addition, there are some adsorption models based on the mathematical and statistical concepts, such as Langmuir model, BET model, and D-R model (Langmuir, 1917; Brunauner et al., 1938; Basha et al., 2008; Chen et al., 2019; Huang et al., 2020). D-R model considers that the adsorbent (pore space) surface is uneven and the adsorption process is the pore condensation of adsorbate (gas) filling adsorbent. To the best of our knowledge, there is no application of morphology method for pore condensation simulation published in the literature.

The aim of this study is to use the morphology approach to simulate mercury injection and pore condensation in CT image to comprehensively characterize pore structure. The algorithm improves the computational efficiency and characterization accuracy by performing morphological operations solely on pore space wall voxels, distinguishing simulation in pore spaces with radii of 1 voxel and half voxel explicitly, and introducing the influence of pore space wall roughness on mercury invasion. Note that the gas pore condensation simulation is not concerned with and not competent for the gas pore condensation mechanism and the detailed micro computation. The major contribution of the gas pore condensation simulation is to simulate the pore condensation process in the entire pore space, so as to obtain the general pore radius distribution to supplement the pore throat radius distribution of MICP.

2. Methods

2.1. Optimization of morphological operations

The morphological operations employed in the following simulations are performed on each voxel of CT image, which is a time-consuming process. We first introduce the optimization of morphological operations. The basic computing unit of morphological operation is the spherical structure element (SSE). SSE is a discrete sphere assembled from a set of voxels. The coordinates of the center voxel are defined as $(0, 0, 0)$, and the Euclidean distance from an arbitrary voxel i (with coordinates (x_i, y_i, z_i)) to the center voxel is

$$dist(i, 0) = \sqrt{x_i^2 + y_i^2 + z_i^2} \tag{1}$$

The $dist(i, 0)$ obeys $dist(i, 0) \leqslant R^2$, where R is the integer radius of SSE. The SSEs with $R = 1$ and $R = 2$ (voxel unit) are shown in Fig. 1a and b, respectively. The shape of SSE is evidently self-similar. A set S_e is defined

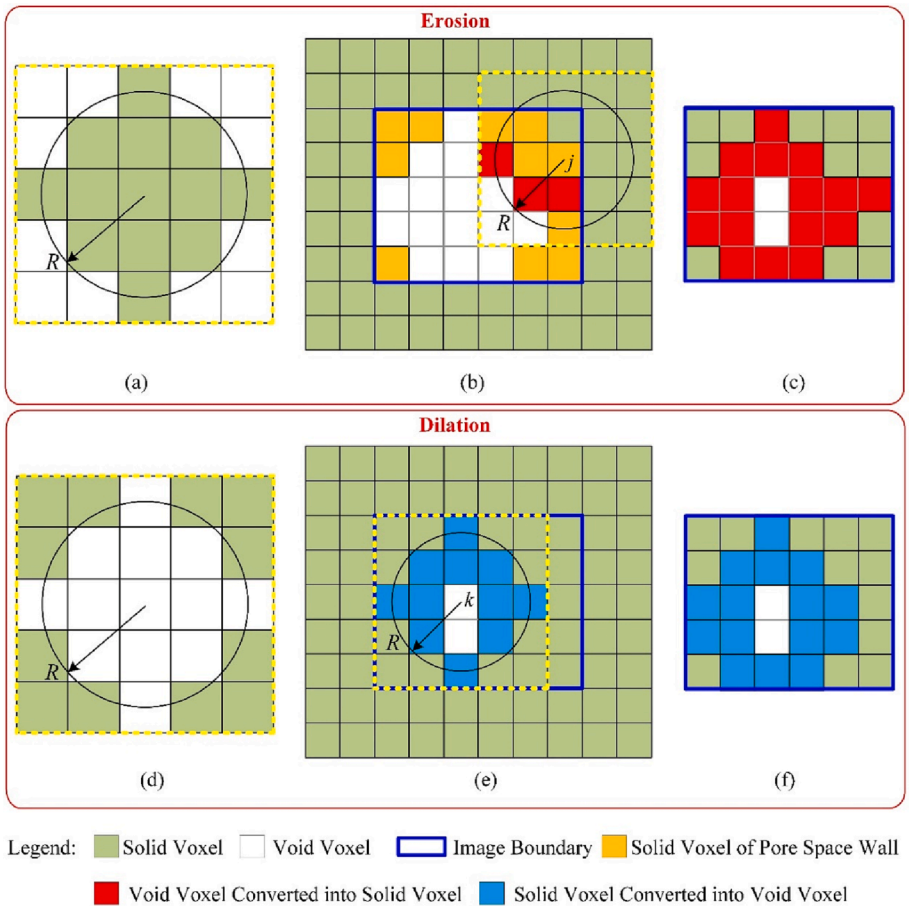

Fig. 2. Schematic of the optimized morphological erosion and dilation operation. (a) S_e stores the SSE consisting of solid voxels. (b) An erosion operation is implemented on a solid voxel j of pore space wall in the binary image via a SSE. Three void voxels in the image whose Euclidean distances from the solid voxel j are less than or equal to R are converted to the solid voxels. (c) The results of the binary image where erosion operation is implemented on each solid voxel of pore space wall. (d) S_e stores the SSE consisting of void voxels. (e) A dilation operation is implemented on a void voxel k of pore space wall in the binary image via a SSE. The solid voxels in the image whose Euclidean distances from the void voxel k are less than or equal to R are converted to the void voxels. (f) The results of the binary image where dilation operation is implemented on each void voxel of pore space wall.

to store the SSE. Fig. 1c shows a XY-cross section of the S_e, in which the SSE with $R = 2$ is stored. The category of voxels inside SSE is opposite to that of voxels outside SSE.

The SSE for the morphological erosion operation is composed of solid voxels (see Fig. 2a) to convert the void voxels into the solid voxels in a binary image. The common erosion operations exert SSEs on each solid voxel of CT image, which poses huge computational amount. In fact, the erosion operation can be implemented by exerting SSEs only on the solid voxels of pore space wall. In order to provide a better understanding of the optimized erosion operation, we use a 2D system to illustrate it. First, the solid voxels of pore space wall are extracted via voxel translation and identification of surrounding voxels (Xu et al., 2020). Then, we make the center voxel of S_e overlap with an arbitrary solid voxel j of pore space wall in the binary image, and perform the logical AND calculation on S_e and the corresponding domain of the binary image. The void voxels in the image whose Euclidean distances from the solid voxel j are less than or equal to R are converted to the solid voxels (see Fig. 2b). Note that it is necessary to add solid voxels to the outside of the image boundary to prevent the S_e overflow in the calculation. The number of layers of the added solid voxels is equal to the radius of the SSE (see Fig. 2b). Fig. 2c shows the results of implementing the erosion operation on each solid voxel of pore space wall in the binary image via SSE with $R = 2$.

The SSE for the morphological dilation operation consists of void voxels (see Fig. 2d) to transform the solid voxels into the void voxels in a binary image. For the eroded binary image shown in Fig. 2c, the void voxels of pore space wall are extracted via voxel translation and identification of surrounding voxels (Xu et al., 2020). Then, the center voxel of S_e is overlapped with an arbitrary void voxel k of pore space wall in the binary image, and the logical OR calculation is performed on S_e and the corresponding domain of the binary image. The solid voxels in the image whose Euclidean distances from the void voxel k are less than or equal to R are transformed into the void voxels, as shown in Fig. 2e. Similar to the erosion calculation, adding solid voxels with the corresponding layers to the outside of the image boundary to prevent the S_e overflow is also necessary. Fig. 2e shows the results of implementing the dilation operation on each void voxel of pore space wall in the binary image via SSE with $R = 2$.

2.2. Simulation of mercury injection capillary pressure

The physical model is a digital porous media with the internal pores saturated with air and the boundary connected to mercury. From the Young-Laplace equation, there is a one-by-one correspondence between the mercury injection pressure and the controlling throat radius, and the mercury invades the internal pores in the order from large pores to small pores, with the increase of injection pressure. We utilize a 2D system to illustrate the simulation, as shown in Fig. 3. Firstly, the erosion operation with R is implemented on the original pore spaces (see Fig. 3b). The pore spaces with radii less than or equal to R are totally converted to the solid matrix (see Fig. 3b and c, pore B and pore D), while the pore spaces with radii larger than R still have some residual voids (see Fig. 3b and c, pore A and pore C). Secondly, we implement the dilation operation with R on the remaining pore spaces (see Fig. 3c). The pore spaces with radii larger than R are restored to their original morphology (see Fig. 3c, pore A and pore C), while the pore spaces with radii less than or equal to R are still solid matrix due to the absence of residual voids for dilation operation (see Fig. 3c, pore B and pore D). The pore spaces converted into solid matrix is the voids that mercury cannot invade under the injection pressure corresponding to R. Thirdly, the connectivity analysis based on 6-adjacencies is performed on the obtained pore spaces with radii larger than R. If a pore space is not connected to the invaded or boundary mercury, the pore space is controlled by the pore spaces with radii less

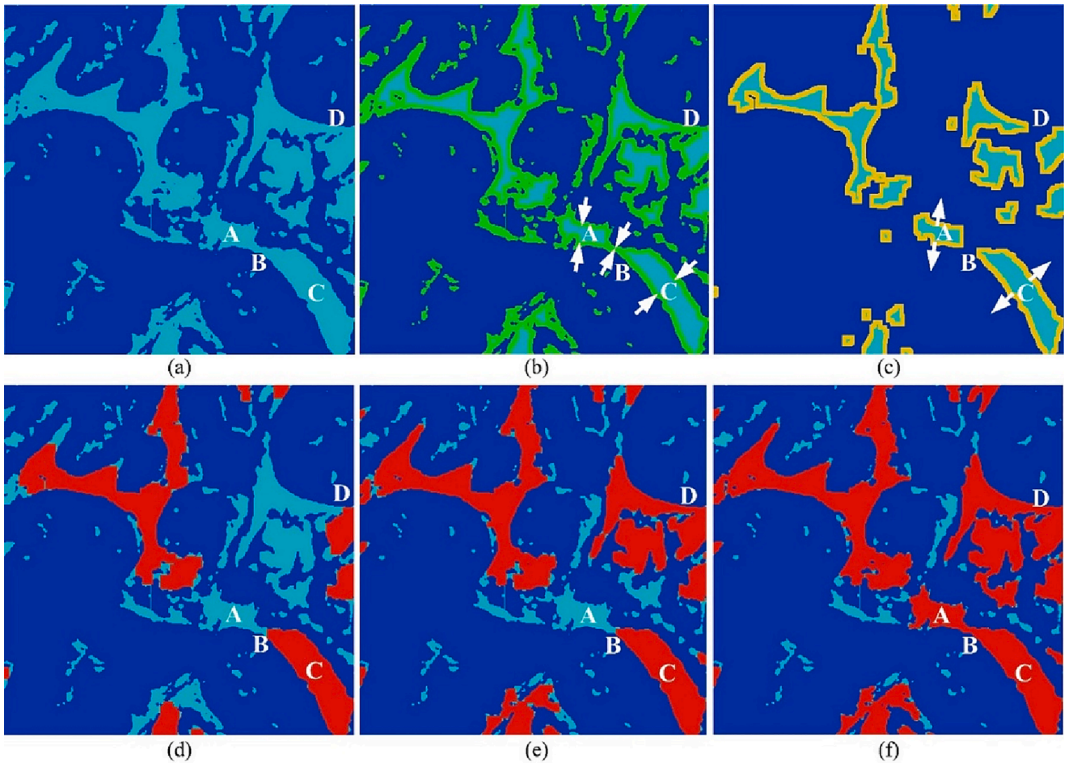

Fig. 3. Schematic of the mercury injection simulation. (a) The original binary image, in which the blue represents solid matrix and the gray denotes pore spaces. (b) The erosion operation where green represents the erosion layer. (c) The dilation operation where yellow represents the dilation layer. (d, e, f) The mercury injection process under the different injection pressure, in which red represents mercury.

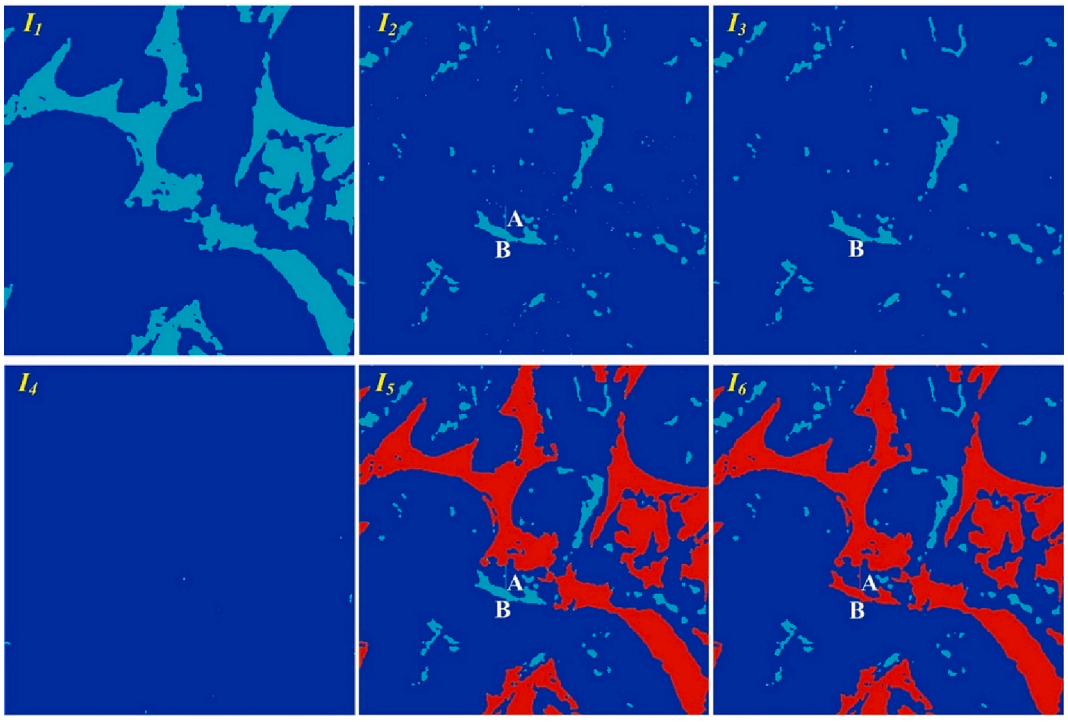

Fig. 4. Schematic of the mercury injection in pore spaces with radius of 1 voxel and pore spaces controlled by them and in pore spaces with radius of half voxel and pore spaces controlled by them, respectively. The image I_1 is obtained after the iteration of $R = 1$. The image I_2 is obtained by exchanging the values of void voxels and solid voxels in I_1 and conducting the logical AND calculation with the original image. The image I_3 is obtained by removing the pore spaces with radius of half voxel. The image I_4 is obtained by performing the connectivity analysis for the remaining pore spaces and mercury in I_3. The image I_5 shows the further mercury injection in pore spaces with radius of 1 voxel and pore spaces controlled by them. The image I_6 shows the final mercury injection in pore spaces with radius of half voxel and pore spaces controlled by them.

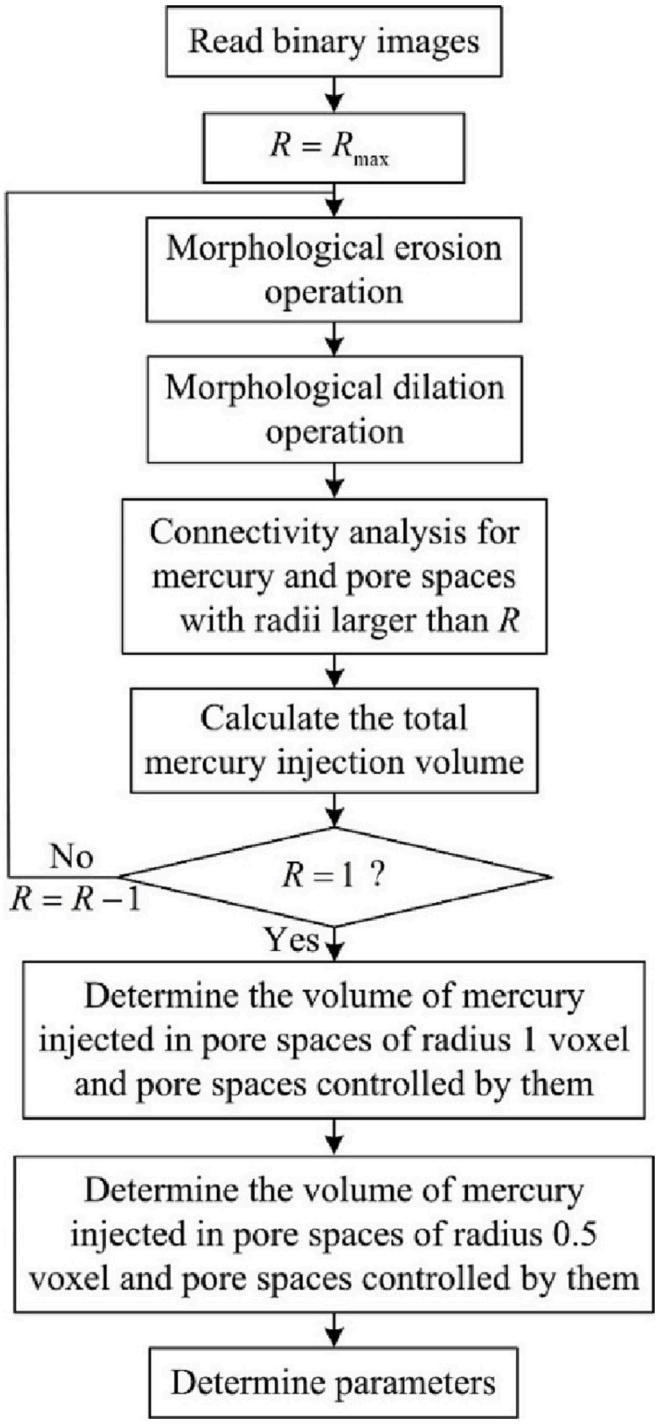

Fig. 5. Workflow of the mercury injection simulation.

than or equal to R, and cannot be invaded by mercury under the injection pressure corresponding to R (see Fig. 3c and d, pore A). Otherwise, the pore space can be invaded by mercury under the injection pressure corresponding to R (see Fig. 3c and 3d, pore C).

R iterates from large to small to simulate the mercury injection process of injection pressure from low to high. Fig. 3d–f show part of the mercury injection process. The total mercury injection volume V is obtained by calculating the number of voxels of pore spaces invaded by mercury, and the mercury injection saturation is the ratio of V to the number of voxels of the entire pore space. From the Washburn equation, the injection pressure corresponding to the R iteration is calculated by:

$$P_C = \frac{2\sigma\cos\theta}{R} \tag{2}$$

where P_C is the injection pressure, σ and θ are the surface tension and Young contact angle, respectively. Note that the pore space wall is virtually rough, which affects the invasion of mercury. From the Wenzel model, the contact angle θ^* of a drop on a rough surface and the Young contact angle satisfy the formula:

$$\cos\theta^* = f\cos\theta \tag{3}$$

where f is the geometric roughness factor of rough pore space wall, defined as the ratio of the actual area of a rough surface to its apparent area (Wenzel, 1936; Quéré, 2008). In this work, we calculate f for each pore space wall using the characterization algorithm of pore space wall roughness described previously (Xu et al., 2020). The formula (2) is rewritten as:

$$P_c = \frac{2\sigma f\cos\theta}{R} \tag{4}$$

The mercury injection capillary pressure-mercury injection saturation curve is thus acquired. Additionally, through subtracting V of the $R+1$ iteration from V of the current R iteration, the volume of pore spaces with $R+1$ and pore spaces controlled by them is obtained. The pore throat radius distribution is thus obtained.

It should be noted that the simulation cannot distinguish pore spaces with radius of 1 voxel and pore spaces with radius of half voxel, because the SSE only possesses integer radii. In fact, the pore spaces with radii of 1 voxel and half voxel and pore spaces controlled by them are all transformed into solid matrix in the last $R = 1$ iteration, and the existing methods directly regard these pore spaces as pores with radius of 1 voxel. However, there are lots of pores with radius of half voxel and pores controlled by them in the porous media image. It is necessary to distinguish them in the simulation.

The scheme of distinguishing them is illustrated in Fig. 4. After the iteration of $R = 1$, the image I_1 is obtained, which contains only part of the pore spaces with radii larger than 1 voxel. The values of void voxels and solid voxels in I_1 are exchanged to generate an intermediate image. The logical AND calculation is conducted between the intermediate image and the original image (see Fig. 3a) to get the image I_2, which contains pore spaces of radii less than or equal to 1 voxel and pore spaces controlled by them. Then, we determine the number of adjacent void voxels for each void voxel in I_2 based on the 26-adjacencies search. If the number of adjacent void voxels of a void voxel is less than 3, the void voxel belongs to the pore spaces with radius of half voxel (Xu et al., 2020). We convert the searched pore spaces with radius of half voxel into solid matrix (see pore A in I_3), and perform connectivity analysis for the remaining pore spaces (see I_3) and mercury to obtain the image I_4, which contains pore spaces with radius of 1 voxel and pore spaces controlled by them. The further mercury injection in pore spaces with radius of 1 voxel and pore spaces controlled by them is shown in I_5. Finally, the connectivity analysis is conducted on pore spaces that are not invaded by mercury in I_5 to implement the final mercury injection in pore spaces with radius of half voxel and pore spaces controlled by them (see pore A and pore B in I_6). Note that some isolated pore spaces in I_6 cannot be invaded by mercury.

Fig. 5 provides the entire workflow of the simulation of mercury injection capillary pressure. Simulation iterates from $R = R_{max}$ to radius of half voxel, which corresponds to the mercury injection process with pressure from small to large. Finally, the pore throat radius distribution and the capillary pressure–saturation curve are obtained. We determine the maximum radius R_{max} by converting the entire pore space into solid matrix in the erosion operation.

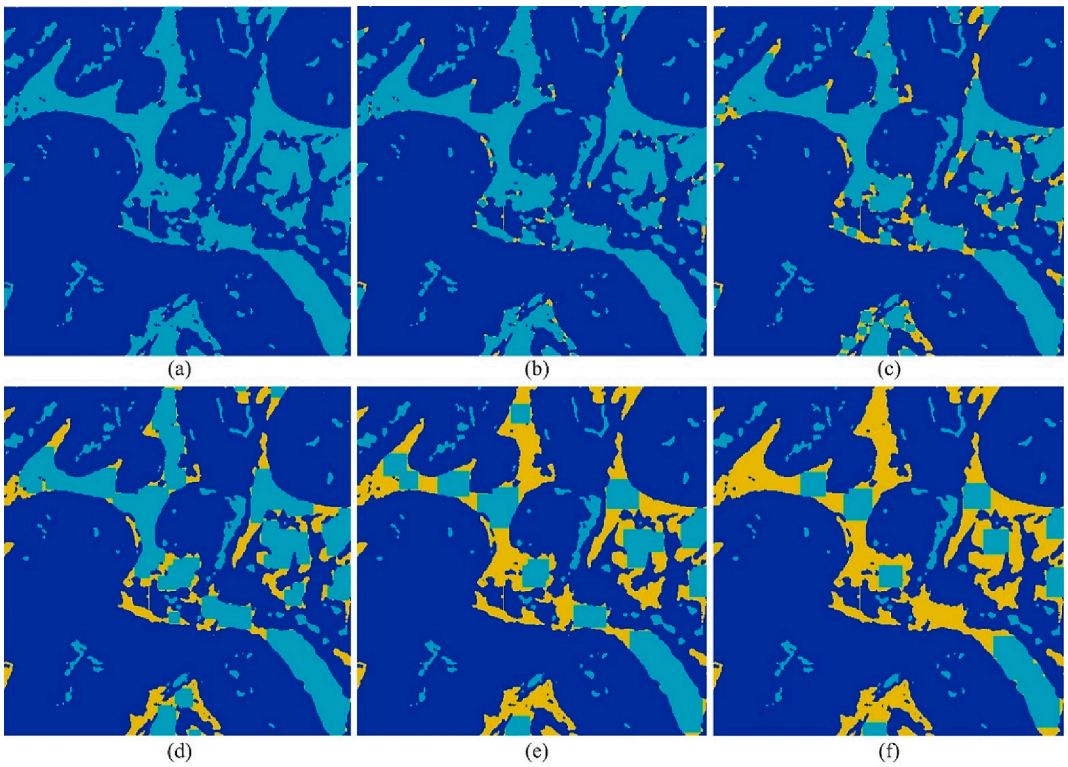

Fig. 6. Schematic of the gas pore condensation simulation. The blue and gray represent the solid matrix and pore spaces, respectively. The orange represents gas. (a, b, c, d, e, f) The gas pore condensation process under the different gas relative pressure.

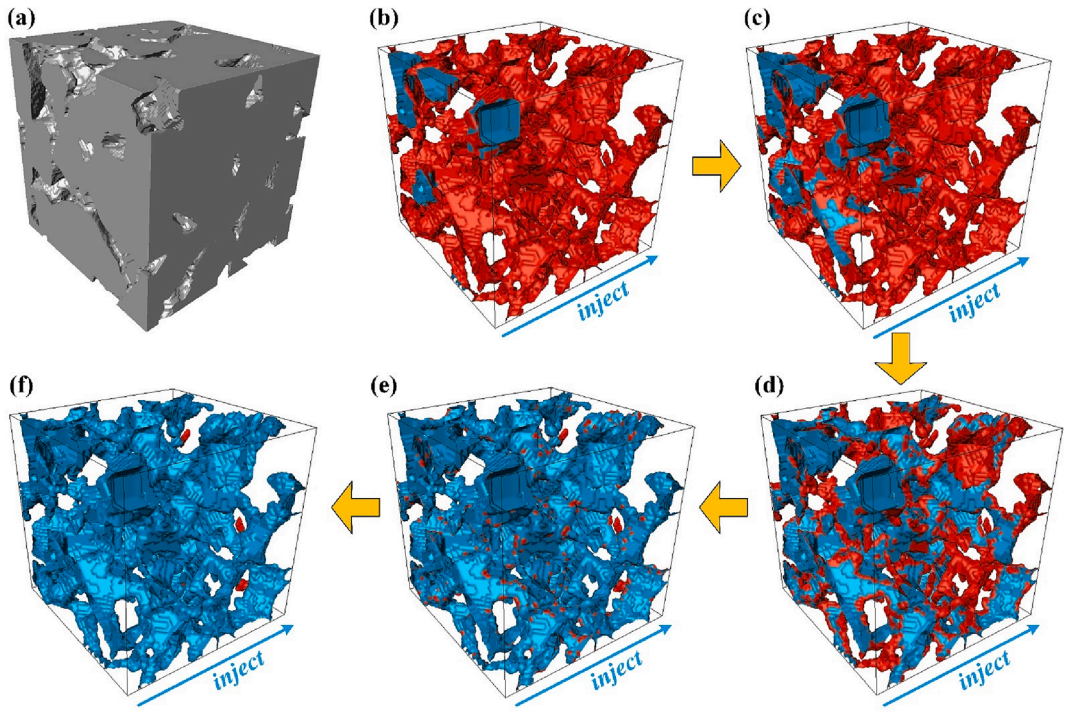

Fig. 7. The visualized mercury injection simulation. (a) A representative porous media image. (b, c, d, e, f) The mercury injection process at different injection pressure. The light blue and red denote mercury and pore spaces, respectively.

2.3. Simulation of gas pore condensation

According to the D-R model, the adsorption process is the pore condensation of adsorbate (gas) filling adsorbent (pore spaces). The gas first condenses in the small pores and fills the small pores, and then condenses in the large pores and fills the large pores with increase of relative pressure. The pore-morphology-based algorithm is conducted based on the voxel, which is crude and cannot precisely describe the process and mechanism of adsorption. The major contribution of this algorithm is to simulate the pore condensation process in the entire pore

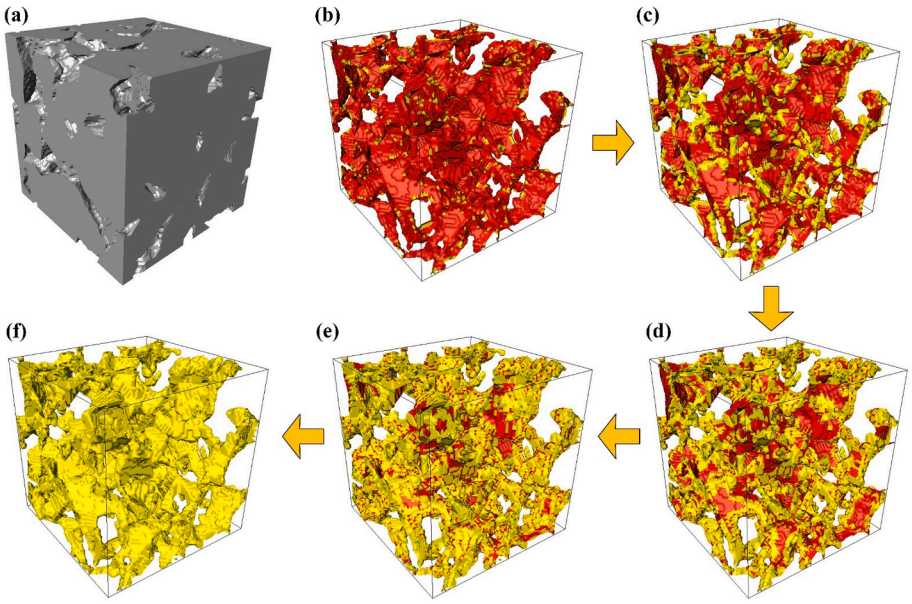

Fig. 8. The visualized pore condensation simulation. (a) A representative porous media image. (b, c, d, e, f) The pore condensation process under the different gas relative pressure. The yellow and red denote gas and pore spaces, respectively.

Table 1
Basic properties of the studied 12 porous media.

Sample	Berea	S1	S2	S3	S4	S5	S6	S7	S8	S9	C1	C2
Type	SA	SA	SA	SA	SA	SA	SA	SA	SA	SA	CA	CA
Size (mm^3)	2.14^3	2.60^3	1.49^3	2.73^3	2.69^3	1.20^3	1.53^3	1.44^3	1.47^3	1.02^3	1.14^3	2.14^3
Porosity	0.196	0.141	0.246	0.168	0.171	0.211	0.239	0.250	0.339	0.221	0.232	0.168

SA and CA represent sandstone and carbonate, respectively.

space of porous media image, so as to obtain the general pore radius distribution to supplement the results of mercury injection simulation.

The physical model is a digital porous media with the internal vacuum pores and the boundary connected to a gas, such as nitrogen. From the Kelvin equation:

$$\ln\left(\frac{p}{p_0}\right) = -\frac{2\sigma V_m}{R_g T R} \tag{5}$$

where p and p_0 are the equilibrium vapor pressure and saturated vapor pressure of the gas, respectively. p/p_0 is the gas relative pressure. σ and V_m are the surface tension and molar volume of the gas, respectively. R_g and T are the gas constant and boiling point temperature of the gas, respectively. There is a one-by-one correspondence between the gas relative pressure and the pore size, and the gas condenses in the internal pores in the order from small pores to large pores with the increase of gas relative pressure. Moreover, unlike the mercury injection process where the mercury first invades the large pores and is controlled by the small pores, the gas condenses preferentially in the small pores and is not dominated by the large pores during the adsorption process. A 2D system is employed to illustrate the simulation, as shown in Fig. 6. Firstly, the connectivity analysis based on 6-adjacencies is conducted on the entire pore space to obtain the pore spaces connected to the boundary. Secondly, the pore spaces with radius of half voxel and 1 voxel, respectively, are obtained using the above morphological distinguishing algorithm. The gas condenses successively in pore spaces of radius half voxel and then of 1 voxel, as shown in Fig. 6a and b. Thirdly, R iterates from 1 voxel to R_{max} on the connected pore spaces using the above morphological algorithm, which corresponds to the gas pore condensation process with relative pressure from small to large. In each iteration, the pore spaces with radius of $R+1$ are obtained, and the gas fills them. Fig. 6c–f shows this simulation process. By subtracting volume of the $R+1$ iteration from volume of the current R iteration, the volume of pore spaces with $R+1$ is obtained. Finally, the general pore radius distribution is acquired.

3. Results and discussion

3.1. Characterization of pore structure

In this subsection, the proposed method was applied to various porous media CT images to evaluate its performance in pore structure characterization. We first simulate the mercury injection process and the pore condensation process in a representative 3D porous media image to provide an insight into the developed method. Some processes of the mercury injection and the pore condensation are visualized in Figs. 7 and 8, respectively. In order to better illustrate the mercury injection simulation process, the mercury was injected into the image only from the left side (Fig. 7). Note that the mercury can be injected into porous media image from different sides in our method, such as from any side of the image, from any several sides of the image simultaneously. Mercury injection simulation is implemented from six sides of the image simultaneously, when characterizing pore structures.

As shown in Fig. 7, the developed method successfully reproduces mercury injection process in the porous media image. Mercury first invades into the macropores on the left side of porous media image under the given injection pressure (Fig. 7b). With the increase of injection pressure, the internal throats with corresponding radius connected to mercury are broken through, and thus mercury invades into pore spaces controlled by these throats (Fig. 7c and d). Fig. 7e and f show the process of mercury injection in pores with radius of half voxel and pores controlled by them, which is not considered individually in the existing methods. As can be seen from Fig. 7 there are many pores with radius of

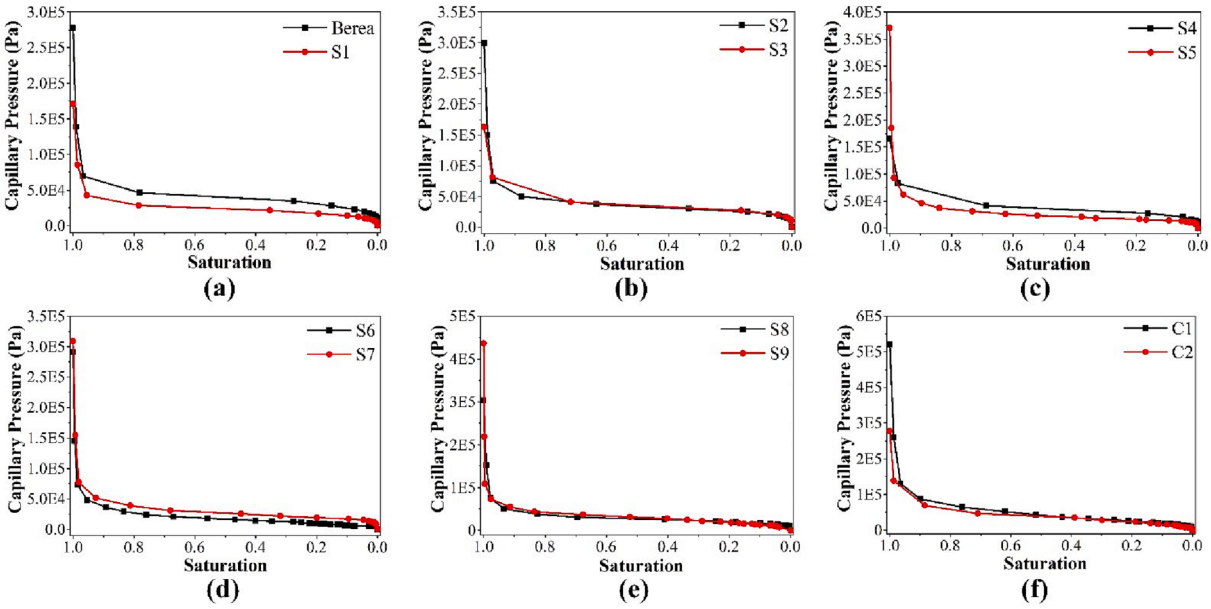

Fig. 9. Capillary pressure–saturation curves of 12 porous media images.

half voxel and pore spaces controlled by them, therefore, it is necessary to explicitly distinguish these pores in the simulation to improve the characterization accuracy. From Fig. 7f, there are some residual pores without mercury, indicating that these pores are isolated pores in the mercury injection direction.

As can be seen from Fig. 8, the developed method also reproduces the pore condensation process in the porous media image. According to the D-R model, gas first enters the micropores connected to the boundary from all sides of image and condenses in the micropores under the given gas relative pressure. As gas relative pressure increases, gas enters the macropores connected to the micropores and condenses in the macropores.

Twelve porous media images are used for pore structure characterization via the developed method. The 12 images are obtained from the open sources of Imperial College London (Dong and Blunt, 2009). The basic properties of the 12 porous media were summarized in Table 1.

We set θ and σ of mercury to 140^0 and 0.4842 $N/$m, respectively. The calculated capillary pressure–saturation curves of 12 porous media images are shown in Fig. 9. As can be seen, the calculated capillary pressure–saturation curves well exhibit the characteristics of capillary pressure curves of sandstones and general carbonates. When the capillary pressure is small, the mercury saturation increases little with the increase of capillary pressure. This result is consistent with the fact that mercury can only invade a small amount of macropores connected to the boundary at the beginning of mercury injection. Then, the mercury saturation shows a significant increase with the continuous rise of capillary pressure, because mercury breaks through the controlling throats and invades a large number of internal pore spaces. From Fig. 9a, the pressure of breaking through controlling throats for Berea is 34.698 kPa, which corresponds to the peak radius of the pore throat radius distribution of Berea (Fig. 10). The pressures of breaking through controlling throats for S6 are various (Fig. 9d) implying that there are several peaks in the pore throat radius distribution of S6 (Fig. 10) and S6 possesses more non-homogeneous pore spaces. Moreover, the residual saturations of the 12 samples are small (Fig. 9) indicating that the 12 samples have good connectivity. The mercury injection simulation is implemented from six sides of image simultaneously, which provides more mercury intrusion paths and leads to small residual saturation. The two leftmost points of capillary pressure curves represent the mercury injection in pores with radius of 1 voxel and pores controlled by them, and in pores with radius of half voxel and pores controlled by them, respectively. It can be seen that the saturation and capillary pressure of the two points have large differences implying that it is necessary to explicitly distinguish these pores in the simulation to improve the characterization accuracy.

Fig. 10 shows the pore throat radius distribution calculated by mercury injection simulation and the general pore radius distribution calculated by gas pore condensation simulation, respectively. As can be seen, both pore throat radius distribution and general pore radius distribution are quite different in the number of peaks, the peak radius, and the pore size range. The general pore radius distribution has more peaks and larger pore size range than the pore throat radius distribution. The reason is that a large number of pores with distinct sizes are controlled by a small throat, and thus these pores are all included in the volume fraction of the small throat in the mercury injection simulation. The general pore radius distribution characterizes the size distribution of each pore, which is pure geometry. The pore throat radius distribution characterizes size distribution of the controlling throats, which is geometric topology. The comprehensive characterization of pore structures needs to integrate the two size distributions. Moreover, the volume fractions of pore spaces with radius of 1 voxel and half voxel have some differences in both two size differences (Fig. 10), implying that it is necessary to explicitly distinguish these pores in the simulation to improve the characterization accuracy. From Fig. 10, it can be seen that S1 and S6 have larger size range of pores than other samples, indicating that the pore spaces of S1 and S6 are more developed.

3.2. *Comparison of simulated results and available results*

We first validate the developed method by comparison with the experimental results. A Bentheimer sandstone (Lin et al., 2018) with porosity of 0.24 is employed. The image of the Bentheimer sandstone is in Appendix A. The resolution and dimension of the porous media are 3.578 *um* and $3.578 \times 3.578 \times 10.734 mm^3$, respectively.

The capillary pressure–saturation curves calculated from the image (Appendix A) using the developed method are compared with the MICP experimental results in Fig. 11. As can be seen, the capillary pressure curves are consistent with the experimental results, although the residual saturation was slightly less than the experimental results when the curve became steep with the rapid rise of capillary pressure. This could be due to the fact that the transport of mercury in the corners of pores were not considered individually. Fig. 12 shows the spatial

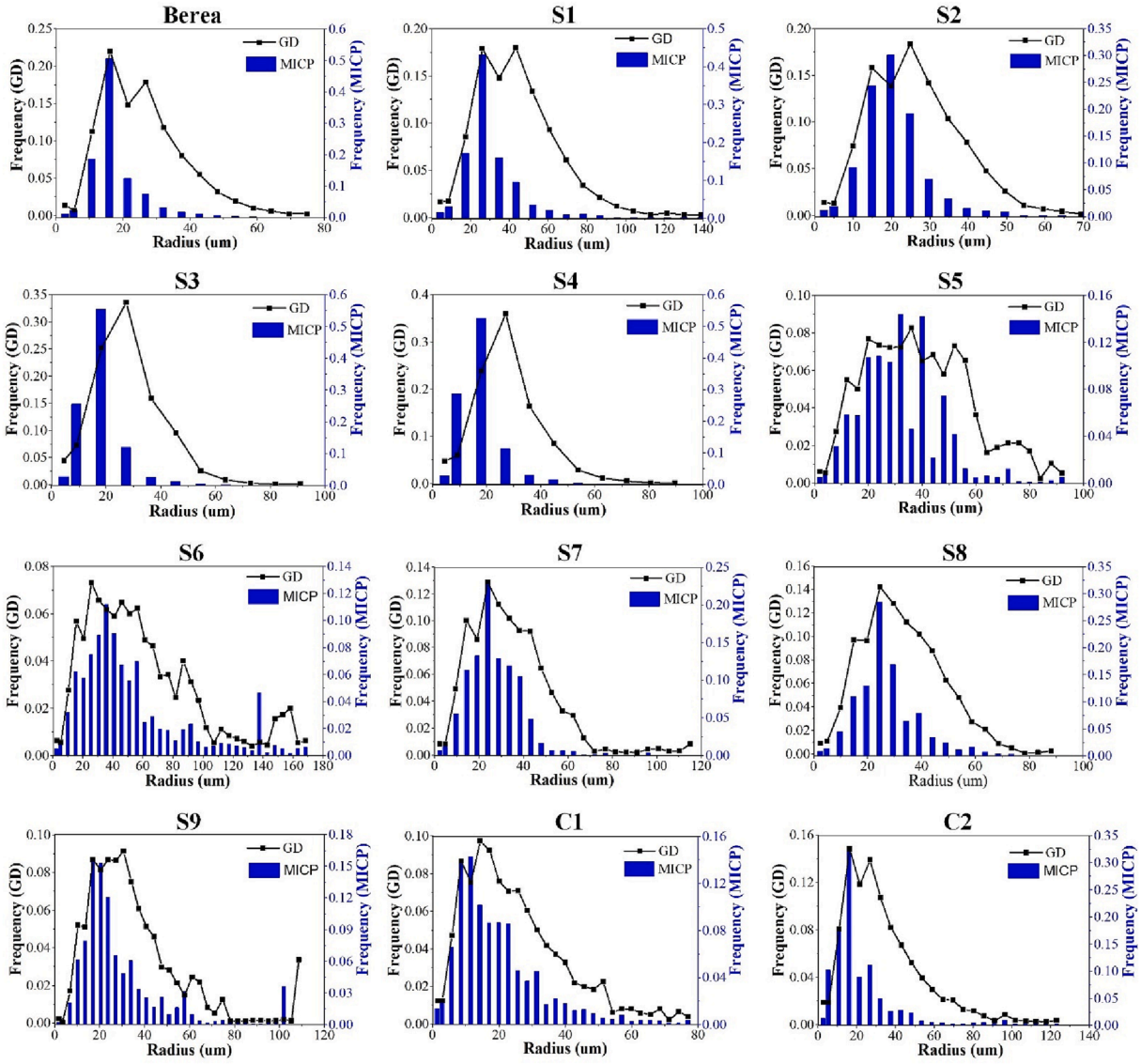

Fig. 10. The pore throat radius distribution and general pore radius distribution of 12 porous media images.

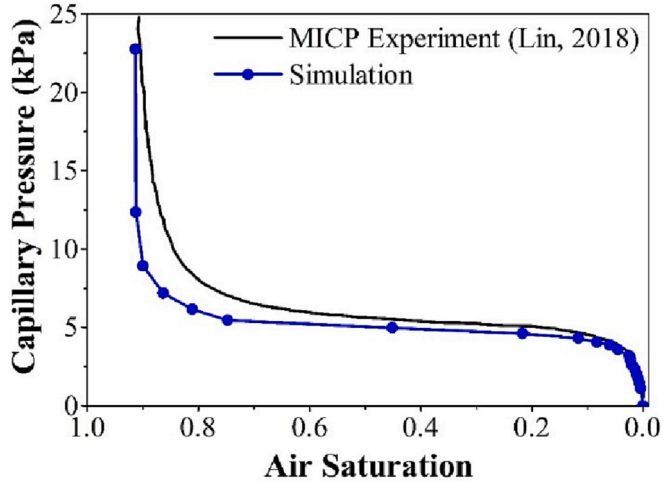

Fig. 11. The calculated capillary pressure–saturation curve is compared to the MICP experimental results (Lin et al., 2018).

distribution of mercury in the entire pore space at one pressure point. As can be seen from one axial slice in Fig. 12c, the corners of the broken pores are all occupied by mercury, which leads to smaller residual saturation. Furthermore, the image noise and the image threshold segmentation would make some differences between the imaging pore structures and the original pore structures, which would also lead to some errors in the simulation.

The number of voxels of the employed Bentheimer sandstone image is $1000 \times 1000 \times 3000$, which leads to a significant computational challenge in terms of the computational memory and time-consuming. Encouragingly, the developed method is possible to efficiently process this large size image. It indicates that the presented method can efficiently characterize the representative pore structures based on the large size image.

A simple comparison between our calculated results and those in other literature is then implemented (Fig. 13) to analyze the effect of our improved algorithm. The employed packings of spheres are reproduced based on the statistics (Hilpert and Miller, 2001). As can be seen from Fig. 13, the calculated capillary pressure–saturation curves in general are in good agreement with those calculated by Hilpert and Miller (2001). Our results possess higher maximum capillary pressure and finer saturation changes due to the explicit distinction between pores with

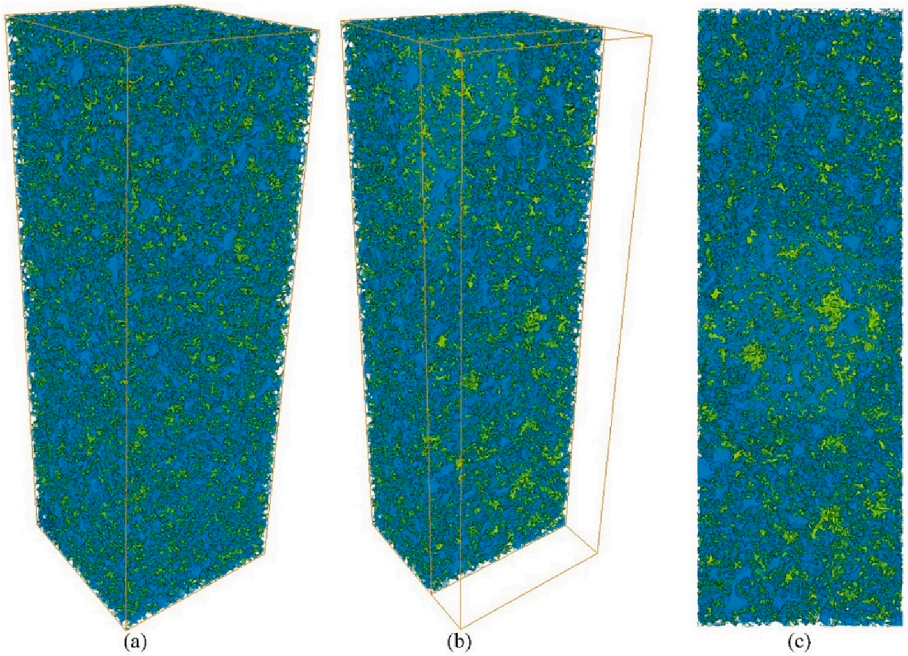

Fig. 12. (a) The visualized spatial distribution of mercury in the entire pore space at one pressure point. (b) The axial sectional view of (a). (c) The axial slice of (b). The blue and yellow represent solid matrix and mercury, respectively.

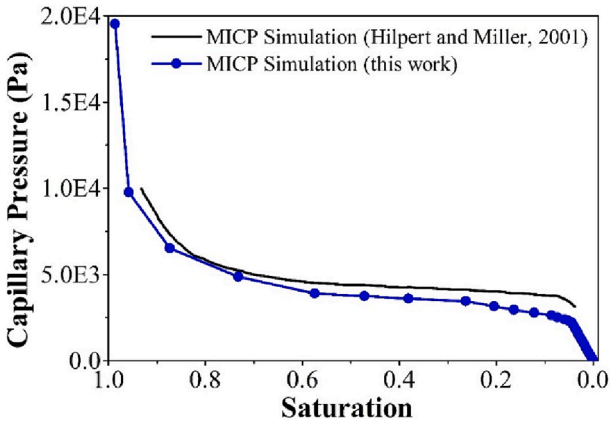

Fig. 13. The calculated capillary pressure–saturation curve is compared to those in Hilpert and Miller (2001).

radius of half voxel and 1voxel.

Identification of pore and throat is the process of detecting and dividing the irregular pore space into a system of pores connected by throats, in which the strict throat radius distribution can be obtained (Jiang et al., 2007; Dong and Blunt, 2009; Yi et al., 2017; Xu et al., 2020). MB (Maximal Ball) and PTM (Pore-Throat Morphology) are the two common high-precision pore and throat identification algorithms (Dong and Blunt, 2009; Xu et al., 2020). MB uses a series of maximal balls to approach pore space and then these balls are affiliated into family trees to define pores and throats. PTM applies the full morphology algorithm to identify the pores and throats based on their morphological features. In order to discuss differences between the pore throat radius distribution obtained by mercury injection and the strict throat radius distribution, the pore throat radius distributions of our method are compared to the strict throat radius distributions of MB and PTM (Fig. 14). The comparison was implemented on the studied 12 samples employed in Subsection 3.1 to provide more insight of these two distributions.

Fig. 14 shows that the pore throat radius distributions of MICP were in good agreement with the strict throat radius distribution of MB and PTM for Berea, S1, C1, and C2. In fact, the four samples also have homogeneous pore spaces. For S2, S3, S4, S7, S8, and S9, the peak pore throat radii of MICP were slightly different from the results of MB and PTM. However, the pore throat radius distributions of MICP were the most different from the strict throat radius distributions of MB and PTM for S5 and S6. From the analysis of pore structure characteristics in Subsection 3.1, the two samples have more non-homogeneous pore spaces. It indicates that the pore throat radius distribution obtained by mercury injection can generally characterize the throat properties located at hydraulic restrictions of pore structure. However, it is necessary to characterize pore structure via synthesizing several information for samples with heterogeneity, because the pore throat radius distributions obtained by mercury injection were different from the strict throat radius distributions.

3.3. Discussion

In order to further assess the performance of the developed algorithm in characterization of strong heterogeneous pore structures, a marine shale from Longmaxi formation, Sichuan, China is employed here. Fig. 15a shows the shale images with the voxel number of $1024 \times 744 \times 406$, and the voxel size is 10 nm. The light grey represents inorganic matrix, and the dark grey is kerogen in which the darkest parts are organic pores. Kerogen with developed organic pores in general is the primary focus. We extract three kerogen parts from shale images and perform the MICP simulation and gas pore condensation simulation in them. Fig. 15b, c, and d show the organic pores in the three kerogens.

The calculated capillary pressure–saturation curves are shown in Fig. 15e–g. As can be seen, the calculated results well exhibit the characteristics of capillary pressure curves of shale. The capillary pressure is much high due to the development of nanopores. The maximum capillary pressure is 148.3 MPa, which corresponds to the controlling throats with radius of 5 nm (half voxel). A large amount of pore spaces is controlled by the controlling throat, the mercury saturation, therefore, significantly increases from about 0.1 to 0.9, when the mercury injection pressure exceeds the capillary pressure of controlling throat. Fig. 15h–j illustrates the pore throat radius distribution and the general pore radius

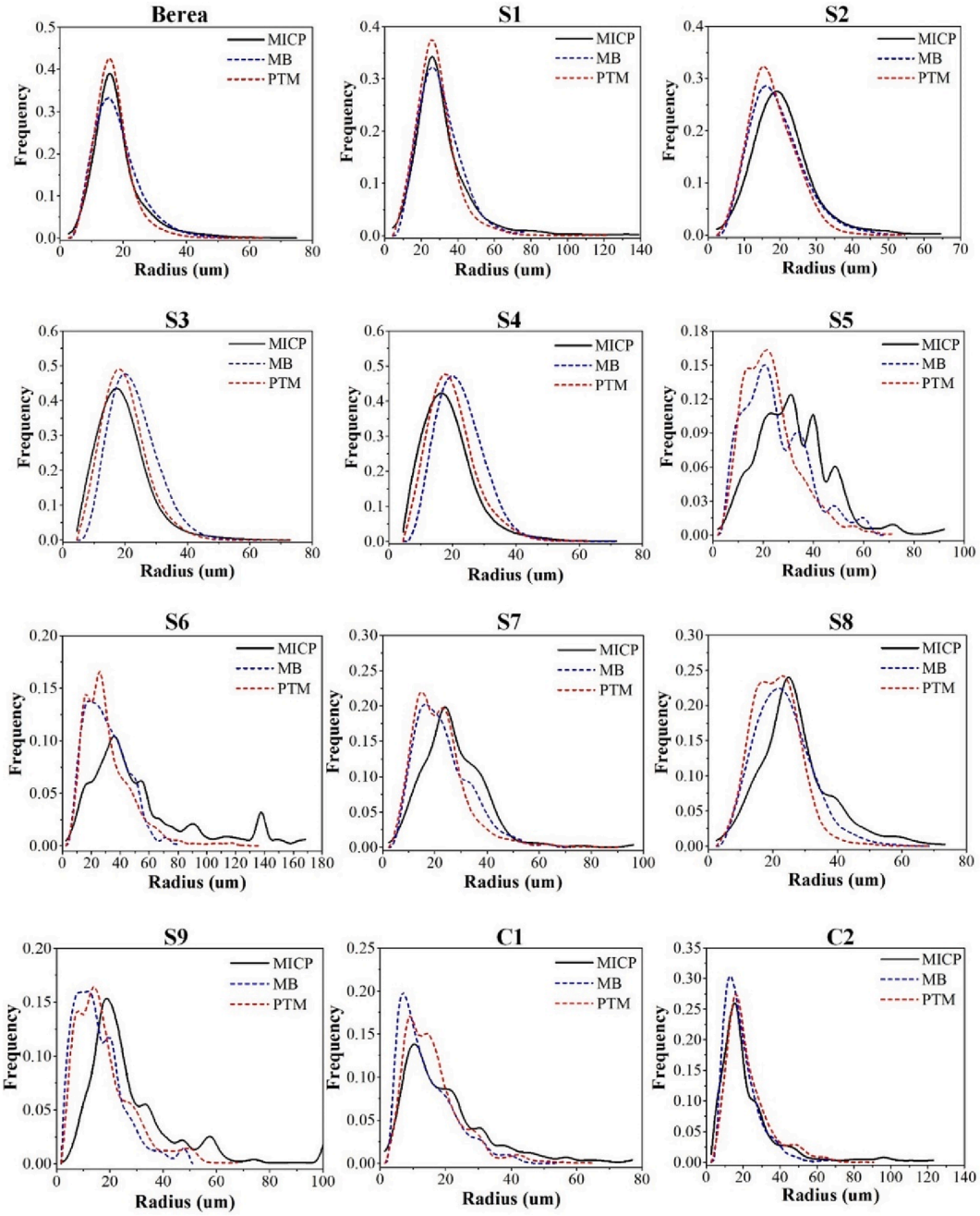

Fig. 14. The comparison between the pore throat radius distributions and the strict throat radius distributions for 12 porous media images.

distribution calculated by the MICP simulation and pore condensation simulation, respectively. The fraction of peak pore throat radius is about 0.8, which is much larger than the fraction of peak pore radius in general pore radius distribution. The phenomenon is consistent with the above observation of mercury saturation increasing from about 0.1 to 0.9 (Fig. 15e–g.), when mercury breaks through the controlling throats. In addition, there are significant differences between the two radius distributions, indicating that the characterization of strong heterogeneous pore structures requires a combination of pure geometric general pore radius distribution and topological pore throat radius distribution. Overall, the developed algorithm can be competent for the characterization of strong heterogeneous pore structures (e.g., shale) based on the images.

The pore space wall of porous media is virtually rough, which affects the invasion of mercury. Taking Berea as an example, the effect of different pore roughness factors on capillary pressure–saturation curve is shown in Fig. 16. As can be seen from Fig. 16a, with the enhancement of pore roughness, the capillary pressure increases at the same saturation. The reason is that the large pore roughness results in large wall resistance, leading to the increase of the difficulty of mercury invading pore spaces.

The entry pressure P_{entry}, median pressure P_{50}, and maximum pressure P_{max} are further calculated from the capillary pressure–saturation curves. P_{entry} is the minimum pressure that can make mercury invade into pore space. P_{50} is defined as the mercury injection pressure when the mercury saturation is 50%. P_{max} is the pressure at the end of mercury invasion. Fig. 16b shows the effect of pore roughness on the three pressures. As can be seen, the three pressures increase with the increase of pore roughness. It indicates that the neglect of pore roughness can lead to the underestimation of capillary pressure in the MICP simulation.

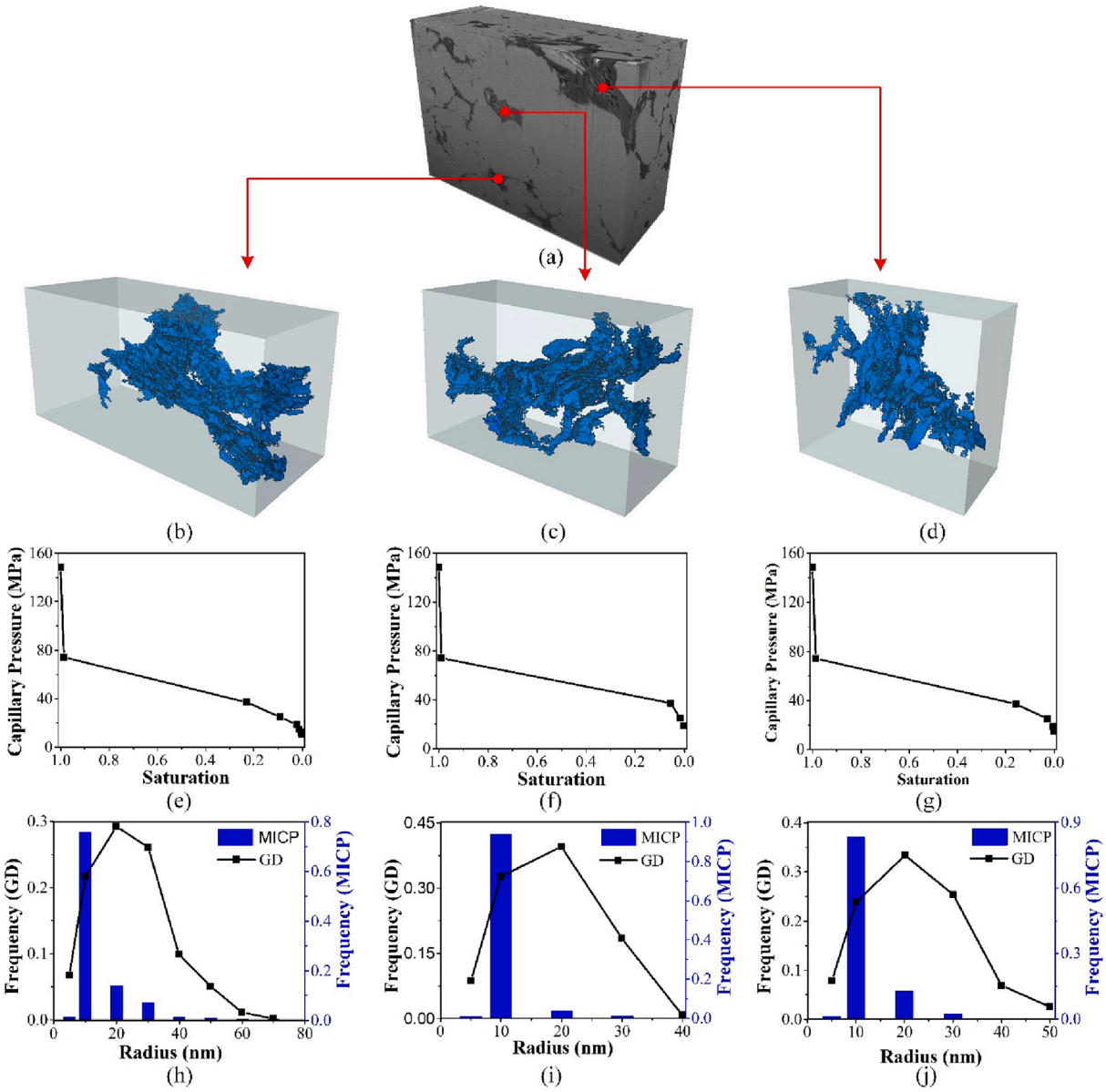

Fig. 15. Characterization of strong heterogeneous pore structures in shale. (a) FIB-SEM images of a real marine shale from Longmaxi formation. The voxel number of the image is 1024 × 744 × 406, and the voxel size is 10 nm. (b)-(d) Pore structures of three Kerogens extracted from the FIB-SEM images. (e)-(f) The capillary pressure–saturation curves calculated from pore structures of (b)-(d), respectively. (h)-(j) The pore throat radius distribution and general pore radius distribution calculated from pore structures of (b)-(d), respectively.

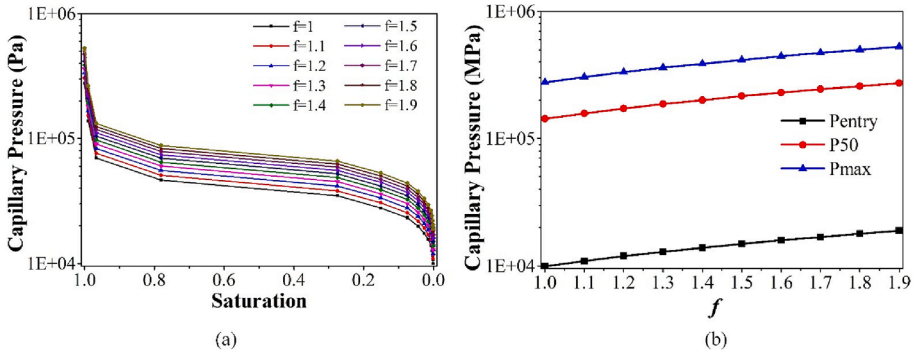

Fig. 16. (a) The effects of pore roughness on capillary pressure–saturation curve. (b) The effects of pore roughness on entry pressure P_{entry}, median pressure P_{50}, and maximum pressure P_{max}.

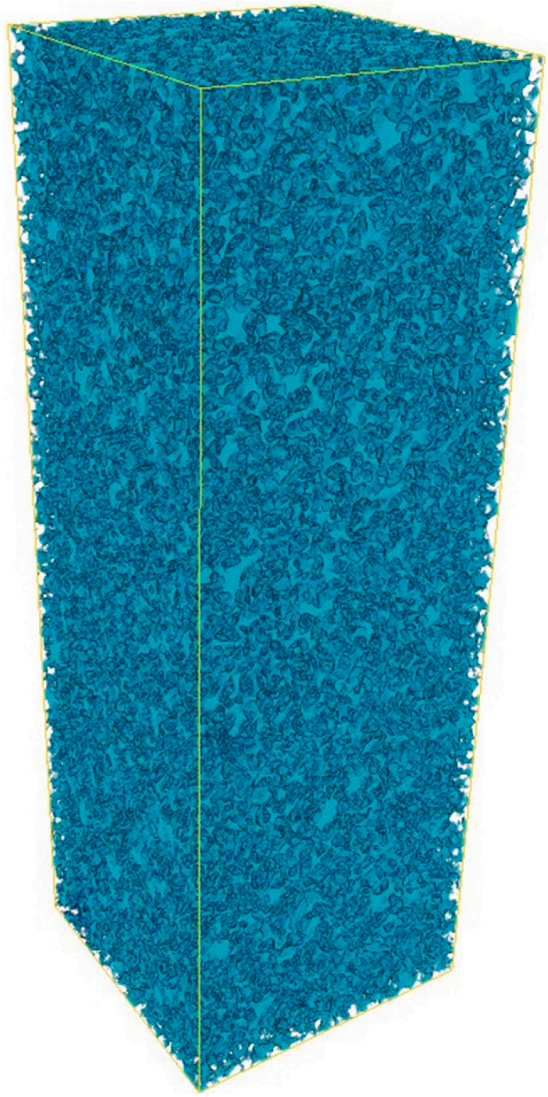

Fig. A1. The Bentheimer sandstone image (Lin et al., 2018). The porosity of the image is 0.24, and the resolution and dimension of the image are 3.578 *um* and $3.578 \times 3.578 \times 10.734 mm^3$, respectively.

And the errors caused by the neglect of pore roughness increases with the increase of pore roughness.

4. Conclusions

In this study, a pore-morphology-based algorithm is proposed to simulate mercury injection and gas pore condensation in CT image to comprehensively characterize pore structure. The algorithm first applies the common morphological operations to the entire pore space to obtain the pore geometry and topology, and then combine with the invasion phase connectivity analysis to implement the mercury injection and gas pore condensation. The capillary pressure–saturation curve and pore throat radius distribution are calculated from the mercury injection simulation, and the general pore radius distribution is acquired from the gas pore condensation simulation. By performing morphological operations solely on pore space wall voxels, distinguishing simulation in pore spaces with radii of 1 voxel and half voxel explicitly, and introducing the influence of pore space wall roughness on mercury invasion, the algorithm improves the computational speed and characterization accuracy. The performance of the algorithm is assessed for various porous media. The pore structure characteristics of various porous media are analyzed. The differences between the general pore radius distribution and pore throat radius distribution are discussed. It is necessary to synthesize the two distributions to comprehensively characterize pore structure. The algorithm is validated by comparing the calculated capillary pressure–saturation curve to the experimental data and the published calculated results. The algorithm can reliably and finely characterize pore structures for a variety of porous media. The pore throat radius distribution and strict throat radius distribution involved in pore structure characterization are clarified. The pore throat radius distribution calculated by mercury injection is consistent with the strict throat radius distribution calculated by pore and throat identification for most porous media. It indicates that the pore throat radius distribution can generally characterize the throat properties located at hydraulic restrictions of pore space for most porous media. However, there are differences between the pore throat radius distributions and the strict throat radius distributions for porous media with heterogeneity. It is necessary to characterize throat properties via synthesizing several information for porous media with strong heterogeneity. The characterization of shale pore structures and the effects of pore roughness on capillary pressure are discussed. The developed algorithm can be competent for the characterization of strong heterogeneous pore structures. And the neglect of pore roughness can lead to the underestimation of capillary pressure in the MICP simulation. The larger the pore roughness, the larger the error caused by the neglect of pore roughness.

It can be concluded that the developed algorithm can reliably, efficiently, comprehensively, and conveniently characterize pore structure for various porous media.

Declaration of Competing Interest

The authors declare that they have no known competing financial interests or personal relationships that could have appeared to influence the work reported in this paper.

Data availability

Data will be made available on request.

Acknowledgements

This work is supported by the National Natural Science Foundation of China (Grant No. 42030808), the Science and Technology Research Project of Henan Province (232102321130), the Strategic Priority Research Program of the Chinese Academy of Sciences (Grant No. XDA14010304).

Appendix A

The Bentheimer sandstone images (Lin et al., 2018) are shown in Fig. A1.

References

An, S., Yao, J., Yang, Y., Zhang, L., Zhao, J., Gao, Y., 2016. Influence of pore structure parameters on flow characteristics based on a digital rock and the pore network model. J. Nat. Gas. Sci. Eng. 31, 156–163. https://doi.org/10.1016/j.jngse.2016.03.009.

Aslannejad, H., Hassanizadeh, S., Raoof, A., de Winter, D., Tomozeiu, N., van Genuchten, M., 2017. Characterizing the hydraulic properties of paper coating layer using FIBSEM tomography and 3D pore-scale modeling. Chem. Eng. Sci. 160, 275–280. https://doi.org/10.1016/j.ces.2016.11.021.

Basha, S., Murthy, Z., Jha, B., 2008. Sorption of Hg (II) from aqueous solutions onto Carica papaya: application of isotherms. Ind. Eng. Chem. Res. 47 (3), 980–986. https://doi.org/10.1016/j.cej.2008.07.005.

Brasili, J., Fox, K., Badamo, D., Berghe, G., Khanal, R., Singh, R., 2019. Molecular dynamics simulation of shale gas confined inside slit-like calcite [104] nanopore. Mol. Simul. 45 (2), 104–110.

Brunauner, S., Emmert, S., Teller, E., 1938. Adsorption of gases in multimolecular layers. J. Am. Chem. Soc. 60 (2), 309–319.

Chen, G., Zhang, J., Lu, S., Pervukhina, M., Liu, K., Xue, Q., Tian, H., Tian, S., Li, J., Clennell, M.B., Dewhurst, D.N., 2016. Adsorption Behavior of Hydrocarbon on Illite. Energy Fuel 30 (11), 9114–9121.

Chen, L., Zuo, L., Jiang, Z., Jiang, S., Liu, K., Tan, J., Zhang, L., 2019. Mechanisms of shale gas adsorption: Evidence from thermodynamics and kinetics study of methane adsorption on shale. Chem. Eng. J. 361 (4), 559–570. https://doi.org/10.1016/j.cej.2018.11.185.

Daigle, H., Hayman, N.W., Jiang, H., Tian, X., Jiang, C., 2017. Multiscale pore networks and their effect on deformation and transport property alteration associated with hydraulic fracturing. Energy Procedia 125, 71–79. https://doi.org/10.1016/J.EGYPRO.2017.08.067.

Dong, H., Blunt, M.J., 2009. Pore-network extraction from micro-computerized-tomography images. Phys. Rev. E. 80 (3), 036307 https://doi.org/10.1103/PhysRevE.80.036307.

Fagbemi, S., Tahmasebi, P., Piri, M., 2018. Interaction between fluid and porous media with complex geometries: a direct pore-scale study. Water Resour. Res. 54 (9), 6336–6356.

Gooya, R., Bruns, S., Müter, D., Moaddel, A., Harti, R.P., Stipp, S.L.S., Sørensen, H.O., 2016. Effect of tomography resolution on the calculated microscopic properties of porous materials: comparison of sandstone and carbonate rocks. Appl. Phys. Lett. 109 (10), 104102 https://doi.org/10.1063/1.4962389.

He, J., Ju, Y., Lammers, L., Kulasinski, K., Zheng, L., 2020. Tortuosity of kerogen pore structure to gas diffusion at molecular- and nano-scales: a molecular dynamics simulation. Chem. Eng. Sci. 215, 115460 https://doi.org/10.1016/j.ces.2019.115460.

Hilpert, M., Miller, C.T., 2001. Pore-morphology-based simulation of drainage in totally wetting porous media. Adv. Water Resour. 24, 243–255. https://doi.org/10.1016/S0309-1708(00)00056-7.

Hilpert, M., Glantz, R., Miller, C.T., 2003. Calibration of a pore-network model by a poremorphological analysis. Transp. Porous Media 51, 267–285. https://doi.org/10.1023/A:1022384431481.

Hu, Q., Zhang, Y., Meng, X., Zheng, L., Xie, Z., Li, M., 2017. Characterization of micro-nano pore networks in shale oil reservoirs of Paleogene Shahejie Formation in Dongying Sag of Bohai Bay Basin, East China. Petrol. Explor. Dev. 44, 720–730. https://doi.org/10.1016/S1876-3804(17)30083-6.

Huang, H., Li, R., Jiang, Z., Li, J., Chen, L., 2020. Investigation of variation in shale gas adsorption capacity with burial depth: Insights from the adsorption potential theory. J. Nat. Gas Sci. Eng. 73 (1), 3043–3054. https://doi.org/10.1016/j.jngse.2019.103043.

Jiang, W., Cao, G., Luo, C., Lin, M., Ji, L., Zhou, J., 2022. A composition-based model for methane adsorption of overmature shales in Wufeng and Longmaxi Formation, Sichuan Basin. Chem. Eng. J. 429, 130766 https://doi.org/10.1016/j.cej.2021.130766.

Jiang, F., Chen, J., Xu, Z., Wang, Z., Hu, T., Chen, D., Li, Q., Li, Y., 2017. Organic matter pore characterization in lacustrine shales with variable maturity using nanometer-scale resolution X-ray computed tomography. Energy Fuel 31 (3), 2669–2680. https://doi.org/10.1021/acs.energyfuels.6b03313.

Jiang, Z., Wu, K., Couples, G., Van Dijke, M.I.J., Sorbie, K.S., Ma, J., 2007. Efficient extraction of networks from three-dimensional porous media. Water Resour. Res. 43, W12S03. https://doi.org/10.1029/2006WR005780.

Krakowska, P., Puskarczyk, E., Jędrychowski, M., Habrat, M., Madejski, P., Dohnalik, M., 2018. Innovative characterization of tight sandstones from Paleozoic basins in Poland using X-ray computed tomography supported by nuclear magnetic resonance and mercury porosimetry. J. Petrol. Sci. Eng. 166, 389–405. https://doi.org/10.1016/j.petrol.2018.03.052.

Langmuir, I., 1917. The adsorption of gases on plane surfaces of glass, mica and platinum. J. Am. Chem. Soc. 40 (9), 1361–1404. https://doi.org/10.1021/ja02242a004.

Lin, Q., Bijeljic, B., Pini, R., Blunt, M.J., Krevor, S., 2018. Imaging and measurement of pore-scale interfacial curvature to determine capillary pressure simultaneously with relative permeability. Water Resour. Res. 54, 7046–7060. https://doi.org/10.1029/2018WR023214.

Matheron, G., 1975. Random Sets and Integral Geometey. Wiley, New York.

Meng, F., 2022. Computed tomography in process engineering. Chem. Eng. Sci. 252, 117272 https://doi.org/10.1016/j.ces.2021.117272.

Mosher, K., He, J., Liu, Y., Rupp, E., Wilcox, J., 2013. Molecular simulation of methane adsorption in micro- and mesoporous carbons with applications to coal and gas shale systems. Int. J. Coal Geol. 109–110, 36–44. https://doi.org/10.1016/j.coal.2013.01.001.

Njiekak, G., Schmitt, D.R., Kofman, R.S., 2018. Pore systems in carbonates formations, Weyburn field, Saskatchewan, Canada: micro-tomography, helium porosimetry and mercury intrusion porosimetry characterization. J. Pet. Sci. Eng. 171, 1496–1513. https://doi.org/10.1061/j.petrol.2018.08.029.

Okolo, G.N., Everson, R.C., Neomagus, H.W.J.P., Roberts, M.J., Sakurovs, R., 2015. Comparing the porosity and surface areas of coal as measured by gas adsorption, mercury intrusion and SAXS techniques. Fuel 141, 293–304. https://doi.org/10.1016/j.fuel.2014.10.046.

Ortiz-Landeros, J., Norton, T., Lin, Y.S., 2013. Effects of support pore structure on carbon dioxide permeation of ceramic-carbonate dual-phase membranes. Chem. Eng. Sci. 104, 891–898. https://doi.org/10.1016/j.ces.2013.09.027.

Quéré, D., 2008. Wetting and roughness. Annu. Rev. Mater. Res. 38, 71–99. https://doi.org/10.1146/annurev.matsci.38.060407.132434.

Serra, J., 1982. Image Analysis and Mathematical Morphology. Academic, London.

Sweijen, T., Aslanneiad, H., Hassanizadeh, S.M., 2017. Capillary pressure-saturation relationships for porous granular materials: pore morphology method vs. pore unit assembly method. Adv. Water Resour. 107, 22–31. https://doi.org/10.1016/j.advwatres.2017.06.001.

Tahmasebi, P., Javadpour, F., Sahimi, M., 2017. Data mining and machine learning for identifying sweet spots in shale reservoirs. Expert Syst. Appl. 88, 435–447. https://doi.org/10.1016/j.eswa.2017.07.015.

Tsakiroglou, C.D., Ioannidis, M.A., Amirtharaj, E., Vizika, O., 2009. A new approach for the characterization of the pore structure of dual porosity rocks. Chem. Eng. Sci. 64 (5), 847–859.

Vogel, H., Tolke, J., Schulz, V., Krafczyk, M., Roth, K., 2005. Comparison of a Lattice-Boltzmann Model, a Full-Morphology Model, and a Pore Network Model for Determining Capillary Pressure–Saturation Relationships. Vadose Zone J. 4 (2), 380–388. https://doi.org/10.2136/vzj2004.0114.

Wenzel, R.N., 1936. Resistance of solid surfaces to wetting by water. Ind. Eng. Chem. 28 (8), 988–994.

Xiong, J., Liu, K., Liu, X., Liang, L., Zeng, Q., 2016. Molecular simulation of methane adsorption in slit-like quartz pores. RSC Adv. 112 (6), 110808–110819. https://doi.org/10.1039/C6RA22803H.

Xu, Z., Lin, M., Jiang, W., Cao, G., Yi, Z., 2020. Identifying the comprehensive pore structure characteristics of a rock from 3D images. J. Petrol. Sci. Eng. 187, 106764 https://doi.org/10.1016/j.petrol.2019.106764.

Yang, F., Hingerl, F.F., Xiao, X., Liu, Y., Wu, Z., Benson, S.M., Toney, M.F., 2015. Extraction of pore-morphology and capillary pressure curves of porous media from synchrotron-based tomography data. Sci. Rep. 5, 10635. https://doi.org/10.1038/srep10635.

Yi, Z., Lin, M., Jiang, W., Zhang, Z., Li, H., Gao, J., 2017. Pore network extraction from pore space images of various porous media systems. Water Resour. Res. 53 (4), 3424–3445. https://doi.org/10.1002/2016WR019272.

Zeng, J., Liu, J.S., Guo, J.C., 2022. Characterization of gas transport in shale: a multi-mechanism permeability modeling approach. Chem. Eng. J. 438, 135604 https://doi.org/10.1016/j.cej.2022.135604.

Zhang, Y., Jiang, F., Tsuji, T., 2022. Influence of pore space heterogeneity on mineral dissolution and permeability evolution investigated using lattice Boltzmann method. Chem. Eng. Sci. 247, 117048.

Zhao, H., Zhao, T., Ning, Z., Zhang, R., Duan, T., Wang, Q., Lian, P., Zhang, D., Zhang, W., 2019. Petrophysical characterization of tight oil sandstones by microscale X-ray computed tomography. Mar. Petrol. Geol. 102, 604–614. https://doi.org/10.1016/j.marpetgeo.2019.01.029.